We are IntechOpen,
the world's leading publisher of
Open Access books
Built by scientists, for scientists

6,900
Open access books available

185,000
International authors and editors

200M
Downloads

Our authors are among the

154
Countries delivered to

TOP 1%
most cited scientists

12.2%
Contributors from top 500 universities

CLARIVATE ANALYTICS
BOOK CITATION INDEX
INDEXED

WEB OF SCIENCE™

Selection of our books indexed in the Book Citation Index
in Web of Science™ Core Collection (BKCI)

Interested in publishing with us?
Contact book.department@intechopen.com

Numbers displayed above are based on latest data collected.
For more information visit www.intechopen.com

Raman Spectroscopy for Monitoring Strain on Graphene and Oxidation Corrosion on Nuclear Claddings

Hongyi Mi, Zhenqiang Ma and James P. Blanchard

Additional information is available at the end of the chapter

Abstract

Raman scattering can explore a material's structure, composition, and condition. In this chapter, we demonstrate the application of Raman scattering to monitor the change in the physical properties and chemical composition of materials. We provide two examples: (1) the Raman peak profile and shift reveal the strain in graphene induced by nanostructure and (2) the appearance and intensity of the Raman peaks indicate the oxidation corrosion on Zircaloy nuclear fuel cladding. The Raman spectroscopy is capable of providing evident and precise signals for the monitoring tasks. Through this research, we propose Raman spectroscopy to be a sensitive, accurate, and nondestructive tool for monitoring material conditions.

Keywords: Raman scattering, phonon vibration, monitoring, mechanical strain, oxidation corrosion, graphene, zirconium alloy nuclear claddings, raman peak intensity, raman shift

1. Introduction

Raman scattering technology is able to reveal phonon/lattice vibrational mechanisms inside materials [1, 2]. By combining this technique with different optical systems, it is feasible for Raman spectroscopy to characterize the physical and chemical changes of materials, including crystal structure deformation and crystal component change [3, 4]. Attributed to its high sensitivity and noncontact detection, the sensing and monitoring applications of the Raman scattering technique for different materials have attracted great interest in both science and engineering fields.

Graphene is a two-dimensional (2D) material consisting of a flat monolayer or several layers of carbon atoms arranged in a honeycomb lattice structure [5, 6]. Because of its special Dirac cone structure which satisfies a linear dispersion relation, graphene has excellent electrical properties, and the charge carriers of graphene can transport as massless Dirac fermions with a mobility up to ~200,000 cm^2 V^{-1} s^{-1} [7–10]. Combined with good mechanical strength [11], outstanding thermal conductivity [12], and excellent optical transparency [13], graphene consequently acts as an attractive candidate for future electronics and photonics applications [14–16]. Previous studies have found that the electrical and thermal characteristics of graphene including electrical resistivity [17], carrier mobility [18], band gap [19], and thermal conductivity [20] are sensitive to mechanical deformation as it alters the structure of the graphene band by confining or collimating the electrons and phonon vibration [19–23]. Therefore, the ability to engineer strain and monitor the mechanical strain condition on graphene is critical in order to fully utilize the electrical properties of graphene.

Through investigating phonon vibrations, Raman spectroscopy has been proven as an important, nondestructive tool to discover the properties of graphene [24, 25]. The mechanical strain can effectively change crystal phonon vibration based on the anharmonicity of the interatomic potentials of the atoms. In other words, the impact of strain on phonon vibration of graphene can be correlated with a change in the Raman characteristic peaks. Several studies using Raman spectroscopy to characterize the phonon vibration of graphene have been carried out with different strains induced by engineering methods [23, 26–29]. The strain on graphene can be clearly reflected in the shift of Raman characteristic peak shifts, and the shift rate is found proportional to the Grüneisen parameter [27, 28].

The management of spent nuclear fuel and other high-level nuclear wastes has drawn great attention from many fields [30]. The growth of an oxide corrosion layer on the cladding, such as zirconium alloy (Zircaloy), is a threat to the nuclear fuel cask storage system, where it may take years for the cladding to cool down due to the slow dissipation of the decay heat [31]. This oxidation process and its product oxide layer are detrimental to the Zircaloy cladding and may play a role in low-temperature creep and delayed hydride cracking [32].

Monitoring of nuclear fuel cladding in dry cask storage can assist with assurance of the integrity of the fuel within the storage canister and is a necessary path to estimate the health of the cladding. Several studies have been performed to understand the oxidation process of Zircaloy [33–36]. More importantly, many detection methods of oxide corrosion have been developed, including environmental monitoring [37], ultrasonic [38], ion beam radiation [39, 40], and optical spectrum methods [41–43]. Compared to other methods, the use of optical spectrum for observation and detection of the oxidation promises to be more flexible, economical, effective, and practical.

As one advanced optical method, Raman scattering technology has been employed to study the properties of zirconium oxide [44–47]. Based on the lattice mechanism, the Raman spectra can be used to identify zirconium oxide from other oxide materials [48] and provide detail of the formation of a textured oxide layer on the Zircaloy cladding [49]. The phonon vibration status of the crystal structure/phase of zirconium oxide (amorphous, tetragonal, and monoclinic polymorphs) can be finely revealed by the Raman characteristic peaks. These previous

studies have resulted in the foundation for further Raman scattering investigation on Zr-4 cladding health conditions and characteristics.

In this chapter, we demonstrated the employment of the Raman scattering technology to monitor the mechanical property changes of graphene and chemical corrosion in zirconium alloy nuclear fuel claddings. The positions, intensities, and profiles of the Raman characteristic peaks precisely and directly probe the physical and chemical changes within these materials. Therefore, Raman spectroscopy is proven to be a nondestructive tool for monitoring material conditions with high sensitivity and high resolution.

2. Raman scattering monitoring of mechanical strain on graphene

To date, several approaches to creating strain in graphene have been proposed [23, 24, 26, 28]. Although the graphene deformation methods are different, the Raman spectroscopy is always accepted as the most powerful and efficient tool to reveal the strain condition on graphene. In this section, we employ Raman scattering technology to observe biaxial strain on monolayer graphene. The strain was induced by deformation from a substrate with an array of SiO_2 nanopillars. The nanopillars (1 cm^2 in area, 80 nm in height, and 40 nm in pitch) were fabricated by employing a self-assembled block copolymer through simple dry etching and deposition processes. The graphene sheet was subsequently transferred to the array of SiO_2 nanopillars. The creation of biaxial tensile strain in graphene was validated based on high-resolution micro-Raman spectroscopy, and the strain values were quantitatively calculated through the Grüneisen parameter. Atomic force microscopy (AFM) and accompanying finite element simulations were employed to confirm the accuracy and reliability of the Raman spectroscopy monitoring results.

Figure 1 shows the schematic process to fabricate SiO_2 nanopillars patterned by self-assembled block copolymer. The fabrication began with forming periodic nanopatterns on 300 nm, thermally grown SiO_2/Si substrate by using a self-assembled block copolymer as a pattern template [50, 51]. A block copolymer layer, poly(styrene-*block*-methyl methacrylate) (PS-b-PMMA), on top of a ~5 nm neutral PS brush layer was used to define periodic nanopatterns (**Figure 1(a)–(c)**). The PMMA cylinders were selectively removed by exposure to UV irradiation and rinsing with acetic acid (CH_3COOH) to form the cylinder-shaped nanopattern template layer. The brush layer in the patterned cylinders was removed by O_2 plasma to allow the following evaporated material to deposit directly to the substrate in the next step. **Figure 2(a)** shows the block copolymer nanotemplate with a pitch (center-to-center distance between cylinders) size ~40 nm. A layer of 15 nm thick chromium (Cr) was deposited by e-beam evaporation and lifted off (**Figure 1(e)–(f)**). The array of Cr nanodots was uniformly created over the entire surface of SiO_2/Si substrate (**Figure 2(b)**). Then, the underlying SiO_2 layer was etched by Cr nanodots as a mask in the inductively coupled plasma (ICP) and the reactive ion etching (RIE) combination system. Finally, an array of SiO_2 nanopillars (80 nm in height and 40 nm in pitch) was formed on Si substrate after removing the Cr nanodots, as shown in **Figure 2(c)**.
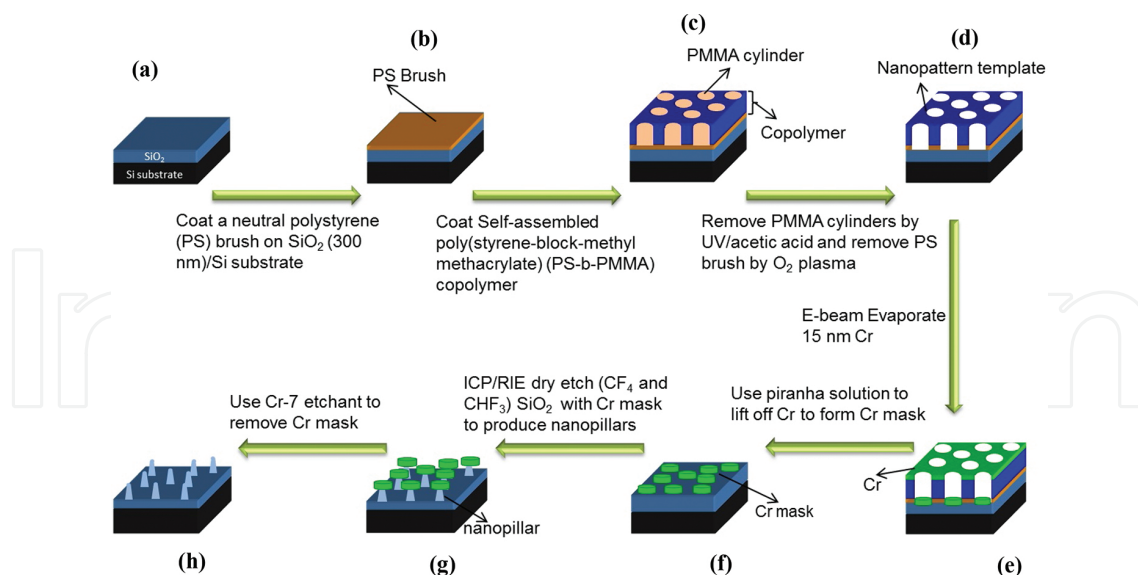
Figure 1. SiO$_2$ nanopillar fabrication process with assistant of self-assembled block copolymer. (a) original SiO$_2$/Si substrate, (b) PS coated on substrate, (c) self-assembled block copolymer coated on PS layer, (d)nanotemplate formed on substrate, (e) Cr evaporated on sample, (f) Cr nanodot on substrate after lift-off, (g) SiO$_2$ nanopillar formed after etching with Cr nanodot mask, and (h) clean SiO$_2$ nanopillar substrate after removing Cr nanodots.
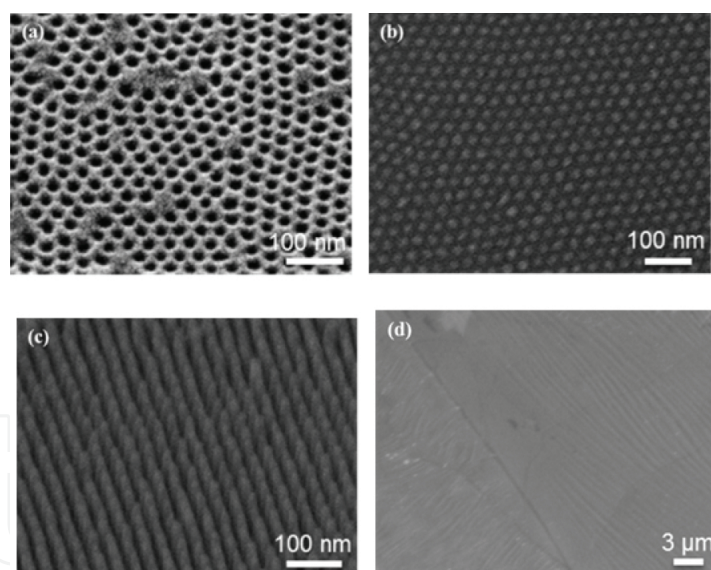

Figure 2. (a) Self-assembled block copolymer nanotemplate on SiO$_2$/Si substrate, (b) Cr nanodots after lift-off on SiO$_2$/Si substrate, (c) obtained SiO$_2$ nanopillars on SiO$_2$/Si substrate, and (d) CVD grown monolayer graphene on Cu foil substrate. From Ref. [52].

The monolayer graphene that was transferred onto the array of SiO$_2$ nanopillars was grown on a 25 μm thick 1″ × 1″ copper (Cu) foil by a chemical vapor deposition (CVD) [53, 54]. **Figure 2(d)** shows the SEM image of the grown monolayer graphene on Cu foil. A layer release-transfer method was employed to transfer the monolayer graphene film onto the pre-prepared SiO$_2$ nanopillar substrate as shown in **Figure 3**.

Firstly, in order to form a 150 nm thick PMMA supporting layer, the graphene layer on the back side of Cu foil was removed by oxygen plasma, followed by spin-coating PMMA on the top side of the graphene sample and baked at 130°C for 3 min (**Figure 3(a)–(c)**). Secondly, the PMMA-coated sample was dipped into 0.25 mol of Fe_3Cl etchant for 4 h to remove the Cu foil completely, and then the left PMMA/graphene membrane was floated on the solution surface (**Figure 3(d)–(e)**). After cleaning the sample in DI water, the floating PMMA/graphene membrane was scooped on the SiO_2 nanopillar substrate, and the PMMA layer was removed by acetone to only leave the graphene film on a SiO_2 nanopillar substrate (**Figure 3(f)–(h)**). The graphene/SiO_2 nanopillar substrate was dried on a hot plate at 105 °C for 1 min to evaporate solvent and water from the sample. With the help of water capillary action and van der Waals forces, the graphene film can be driven to follow the substrate profile. Namely, when the graphene/PMMA film was transferred to the SiO_2 nanopillar substrate, a 150 nm thick PMMA layer made it remain flat on the SiO_2 nanopillars. However, the graphene layer started to sag as the PMMA layer was removed and the capillary action of the water and the van der Waals forces between the graphene layer and the nanopillars helped the graphene layer depress and follow the profile of nanopillars. The schematic illumination for this process is shown in **Figure 4(a)**. During the SiO_2 nanopillar fabrication process, we intentionally left several unpatterned regions on the substrate to attach the graphene film tightly without strain after the transfer, which also can be used as unstrained reference regions in the following Raman spectroscopy study. **Figure 4(b)** is the 45°-angled SEM image showing that the deformed graphene film was supported by numerous and periodic SiO_2 nanopillars.
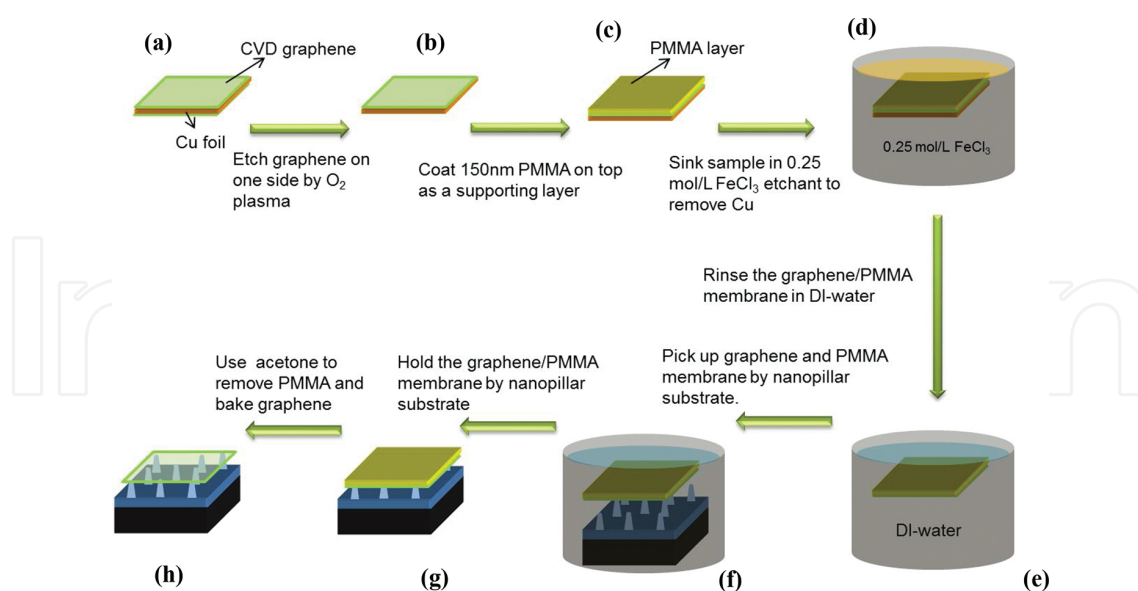

Figure 3. Transfer process of CVD graphene to prepared SiO_2 nanopillar substrate. (a) Graphene grown on Cu foil, (b) sample with back side graphene removed, (c)PMMA coated on graphen, (d) sample sunk in $FeCl_3$ solution to remove Cu, (e) PMMA/graphene layer in DI water for clean, (f) PMMA/graphene layer picked up by prepared SiO_2 nanopiller substrate, (g)Flat PMMA/graphene on top of SiO_2 nanopiller substrate, and (h) deformed graphene on SiO_2 nanopiller after removing PMMA.
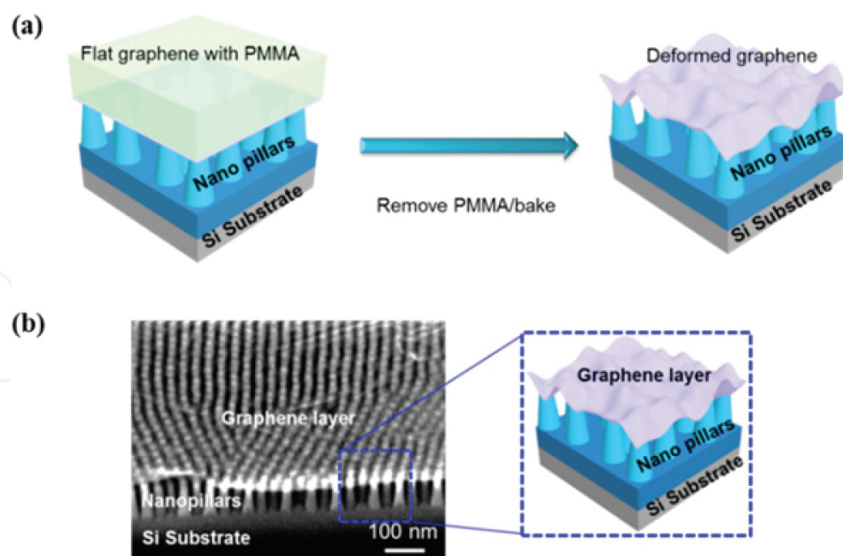
Figure 4. (a) Schematic illumination of graphene deformation process and (b) deformed graphene sheet standing on top of SiO_2 nanopillars.

A Horiba micro-Raman spectrometer (resolution of 0.045 cm^{-1}) with a 50× objective lens (a spot size of about 1 μm) and 18.5 mW of He-Ne (633 nm) was used to investigate the strain on the transferred monolayer graphene. The graphene on both flat regions and the SiO_2 nanopillars was examined at several different positions. From the Raman spectra as shown in **Figure 5(a)** and **(b)**, the intensity of the 2D band is about two times of that of the G band, which is corresponding to monolayer graphene Raman spectra [25, 54]. The graphene on the flat regions (no nanopillars) of the substrate without clear deformation was used as reference to study the strain on graphene. It is clear that there are substantial differences in the Raman spectrum G and 2D bands between the graphene on SiO_2 nanopillars and on the flat region. In **Figure 5(a)** and **(b)**, compared to the flat graphene, there are downshifts in the G band (average shift, 7.8 cm^{-1}) and 2D band (average shift, 16.3 cm^{-1}) of graphene on nanopillars in the peak positions. The downshift of the G band and the 2D band is attributed to the local strain on graphene induced by SiO_2 nanopillars.
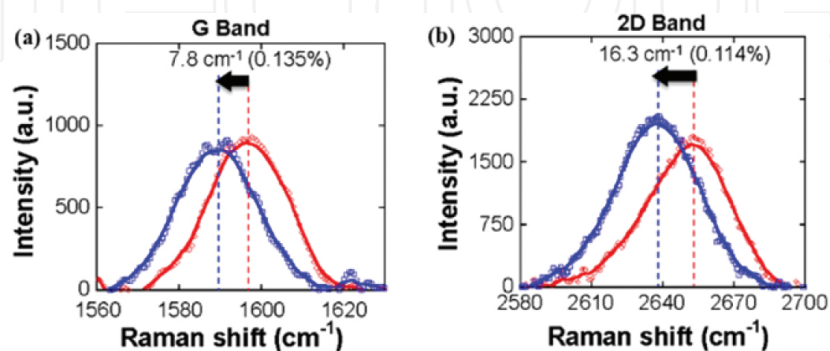

Figure 5. Raman spectra of the (a) G peak downshift and (b) 2D peak downshift taken on the flat surface (red) and on the nanopillars (blue). From Ref. [52].

In the Raman spectra of graphene, the G band is related to the doubly degenerated E_{2g} at the center of the Brillouin zone, while the 2D band is related to the momentum conservation of the scattering of two phonons with opposite waver vectors [26, 27]. The mechanical strain can influence the phonon variation in the crystal [3, 55]. The center-zone phonon vibration change due to the strain is shown in the G band shift, and the change in the double-resonance condition due to the strain, which affects the actual corresponding phonon, can be reflected by the 2D band in the Raman spectrum measurements. The local biaxial tensile strain induced by SiO_2 nanopillar can explain the downshift happening to G and 2D bands.

The Raman shifts were qualitatively studied to discover the biaxial strain through the Grüneisen parameter, which describes the vibrational effect on the crystal lattice property, by the following equation [24, 27, 55]:

$$\gamma = -\frac{1}{\omega_0}\frac{\delta\omega}{\delta\varepsilon_h} \tag{1}$$

where ω_0 is the Raman band frequency without strain, $\delta\omega$ is the Raman band shift, γ is the Grüneisen parameter for the corresponding band, and ε_h is the hydrostatic strain on the graphene film. For biaxial strain, ε_h can be expressed as $\varepsilon_h = \varepsilon_t + \varepsilon_l$ and $\varepsilon_t = \varepsilon_l$, in which ε_t and ε_l are the transversal and longitudinal components of the strain. From Eq. (1), based on previously reported Grüneisen parameters and the downshift characteristic bands collected from the test positions, the biaxial tensile strain $\varepsilon_l = \varepsilon_t$ can be calculated to have an average value of 0.135 % from the G band and 0.117 % from the 2D band.
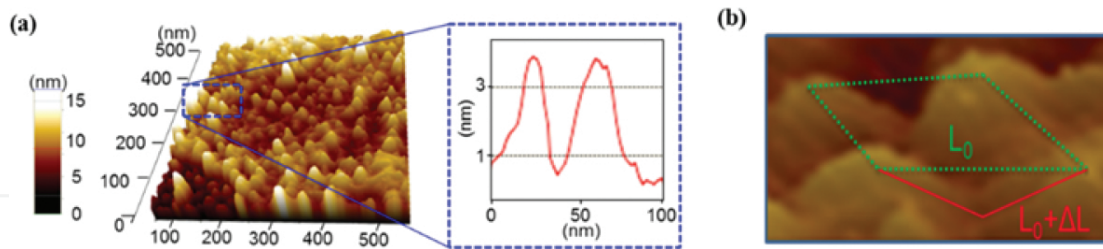

Figure 6. (a) Morphology of the transferred graphene film on the SiO_2 nanopillar substrate measured by AFM and (b) deformed graphene on four adjacent nanopillars (unit area). From Ref. [52].

In order to confirm the Raman spectroscopy defection results, the wavy morphology of the transferred graphene film on the SiO_2 nanopillars substrate was carefully measured by the noncontact-mode atomic force microscopy (AFM) over a 500 nm× 500 nm area as shown in **Figure 6**. It was clearly observed that the surface morphology of the transferred graphene film followed the SiO_2 nanopillar profile. The inserted 2D graphene surface profile in **Figure 6(a)** was taken from two adjacent SiO_2 nanopillars, which indicates how much the graphene layer was deformed. The peak-to-valley distances are found to have a range of about 0.5–5 nm. A subtle difference in the arrangement of the nanopillars and graphene sag condition creates a different degree of deformation on the graphene film. As described in the previous section,

just after transfer, the graphene/PMMA film was kept flat, and the length of the graphene between two pillars was L, while once the PMMA was removed, the graphene began to sag to follow the nanopillar profile, and the length of graphene between two pillars was changed to L + ΔL (**Figure 6(b)**). Then, the mechanical strain on graphene can be calculated by the following equation: strain = ΔL/L [24]. Based on the AFM-measured morphology of the graphene on the nanopillars, the local strain in the graphene can be extracted in the range from about 0.04 to 0.9 % with an average value about 0.17 % measured in a 1 µm^2 area.
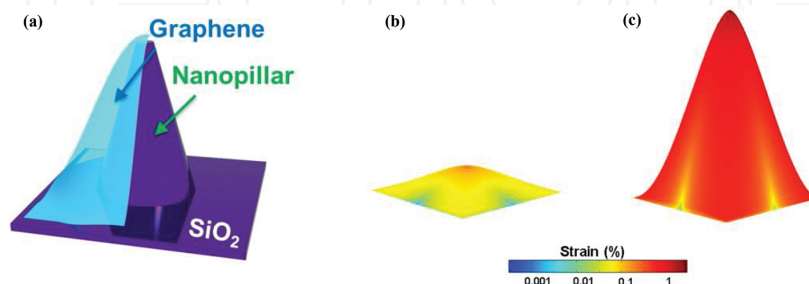

Figure 7. (a) A schematic illustration of strained graphene on top of a nanopillar. Simulated biaxial tensile strain on transferred graphene transferred by COMSOL Multiphysics; (b) with 0.5 nm; and (c) with 5 nm deformation toward. From Ref. [52].
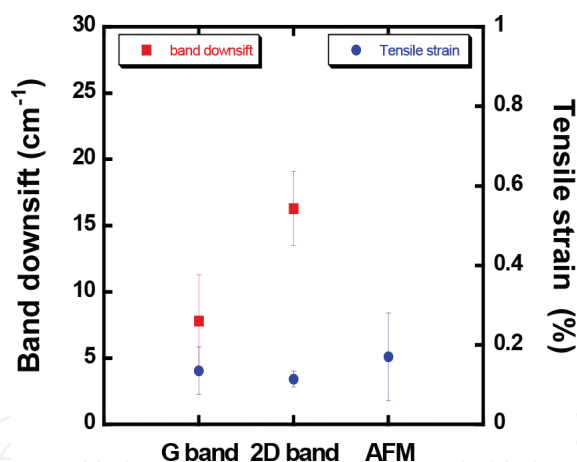

Figure 8. Comparison of the strain extracted from AFM and calculated from Raman band shift.

Furthermore, a strain distribution on graphene based on the deformation values we measured from the AFM was simulated by COMSOL Multiphysics. As shown in **Figure 7(a)**, we used the actual dimensions, structure, and material parameters in the simulation model. For graphene, we used Young's modulus of 1 TPa [11] and Poisson's ratio of 0.3 [56]. We took the two extreme cases, the largest and the smallest deformations which were the 0.5 and 5 nm of the peak-to-valley distances. For the smallest graphene deformation, the maximum strain in the graphene near the top part of the nanopillar is about 0.3 %, and most of the region shows an average strain of about 0.07 % as shown in **Figure 7(b)**. On the other hand, for the largest graphene deformation, the minimum strain in the graphene near the top part of the nanopillar

is as high as 3.5 %, and most of the region shows the average strain about 0.8 % as shown in **Figure 7(c)**. The simulated results confirm the analysis from the AFM measurement.

The Raman shift and strain conditions collected from Raman and AFM are shown in **Figure 8**. This biaxial strain value obtained from Raman spectroscopy detection matched to that obtained from accurate AFM measurement. This result demonstrates the accuracy and effectiveness for the Raman scattering technology to monitor the strain on graphene, even if the strain is induced by subtle nanostructures.

3. Raman scattering monitoring oxidation corrosion of nuclear fuel claddings

Acquiring and understanding the health condition of nuclear fuel cladding are vital for nuclear energy long-term fuel storage systems. In this section, we present the use of Raman scattering technology to monitor oxidation corrosion on nuclear fuel cladding. Systematic Raman scans were performed to study the relationship between typical Raman spectra and various oxidation corrosion layer thicknesses. The thicknesses of the oxide layers were confirmed by cross-sectional scanning electron microscopy (SEM) examination. The results reveal that each oxide layer thickness can be directly related to the Raman scattering characteristic peaks and have proven that Raman scattering technology is an accurate, nondestructive, and sensitive method to monitor the oxidation corrosion of zirconium-based cladding.

The tested Zr-4 cladding samples were cut by saw from 1 mm thick Zr-4 cladding into 1 cm × 1 cm specimens. The Zr-4 samples were ground and polished to remove the native surface oxide layer and provide a smooth sample surface. The morphology of the oxide may be affected by the cold-worked nature of the polished surface. The samples were loaded in a quartz tube with a 5 cm diameter and were oxidized in a Thermo Scientific F79335-70 furnace chamber at 500 °C in flowing air. Samples were oxidized for 5, 10, 20, 50, and 100 h, respectively, to achieve different corrosion layer thicknesses. These oxidation times were chosen such that the thickness of the oxide layer can be clearly distinguished. After oxidation, the polished side of each oxidized sample was ready for f Raman scattering investigation.

The Raman scattering spectra of the oxidized samples were measured with a Thermal Scientific DXR micro-Raman spectrometer. The excitation laser source is a DXR 532 nm green laser, and the output power was 10 mW. The spectra were acquired by a 50 μm aperture. The objective of the microscope was chosen as 10×, providing a laser beam spot size diameter of 2.1 μm. Raman spectra were collected from the entire 2.1 μm diameter spot. The scans implemented a 900 lines/mm grating to obtain full-range spectra and find the interested spectrum range. For each sample, systematic scans for several spots randomly selected at different regions on the sample were carried out. Then, the representative spectra which appeared most frequently were chosen for further analysis.

From the full-range scanned Raman spectra of bare Zr-4 as well as samples oxidized for 5, 10, 20, 50, and 100 h, the characteristic Raman scattering peaks appear between wave number of 160 and 800 cm^{-1}. **Figure 9** shows the selected representative Raman spectra in this wave

number range. A baseline has been subtracted from each spectrum, which allowed all the spectra to be put at the same level to permit selection of the best peaks for measuring the oxide layer thickness. As the Raman spectra reveal, the characteristic Raman scattering peaks become more obvious as the sample's oxidation time increases. In the spectrum from the non-oxidized sample, there is only one peak around 480 cm^{-1} with a very weak intensity. The spectrum from the 5 h sample exhibits the 480 cm^{-1} peak, which is similar to the bare sample. Meanwhile, two weak peaks around 180 and 630 cm^{-1} appear with a broad peak width. In the spectrum from the 10 h sample, the peaks at 180, 480, and 630 cm^{-1} become stronger and wider. In addition, two peaks at 340 and 380 cm^{-1} appear. The spectrum from the 20 h sample is similar to that of the 10 h sample, but the intensity of each peak increases slightly. The peaks at 180 and 630 cm^{-1} begin to split into two sub-peaks at 175 and 187 cm^{-1} and 613 and 638 cm^{-1}, respectively. In the spectrum from the 50 h sample, all these peaks still exist at the same positions but with much stronger intensities. New peaks at 220, 540, and 580 cm^{-1} also appear within this spectrum. The spectrum from the 100 h sample contains all the peaks in the 50 h sample's spectrum, but each of them displays an increase in intensity. Furthermore, there are two new peaks at 280 and 300 cm^{-1} with weak intensities.
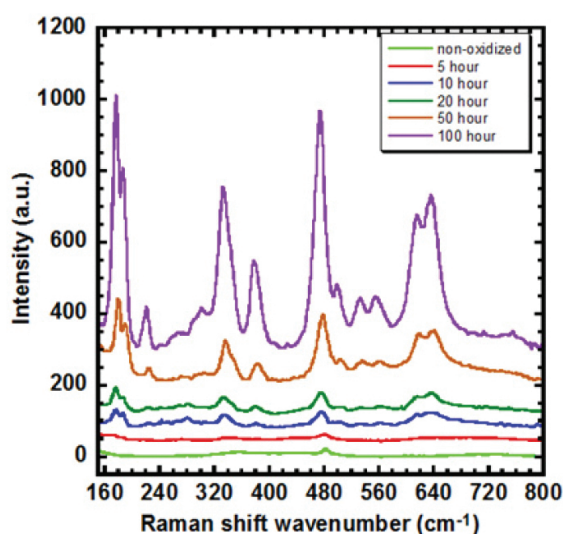

Figure 9. The selected representative Raman spectra of the non-oxidized, 5, 10, 20, 50, and 100 h oxidized Zr-4 cladding samples. As the oxidation time increases, there are 12 characteristic peaks appearing in the spectra. From Ref. [58].

As the oxidation time increases, a thicker oxide layer is grown on top of Zr-4, and in turn, the Raman spectrum of this sample can show stronger Raman scattering signals. Comparing all of these Raman spectra in detail, some characteristic peaks are helpful in identifying bare and oxidized samples. As discussed previously, there are 12 characteristic peaks appearing or enhanced in the spectra of the tested samples. In the spectra of the bare and 5 h samples, the differences are only observed for peaks at 180 and 630 cm^{-1}, which do not exist in the bare sample spectrum. These two peaks exist in all the spectra of the oxidized samples (from 5 to 100 h), and their intensities increase consistently as the oxidation time increases, although there is splitting happening in these two peaks for samples exposed for longer times. These split

peaks at 175, 187, 613, and 638 cm^{-1} correspond to the existence of the zirconium oxide tetragonal and monoclinic polymorphs in the oxide layer [44, 57]. When an oxide layer grows thicker, there will be more zirconium oxide in these polymorphs. Oxide layers grown in environments other than air will likely have a different morphology than those studied here. Future work is necessary to establish whether the approach used successfully in this study will apply to oxides grown under other conditions.

After the Raman spectrum measurement, the oxidized Zr-4 samples were prepared with phenolic mount for cross section measurement by SEM in order to examine the Raman results. Because of the different properties of phenolic, zirconium oxide, and Zr-4, these three materials can be easily distinguished by the white-black contrast. Zirconium oxide is a high dielectric constant material, so compared with Zr-4, the zirconium oxide layer has a darker gray color in SEM images, and the boundary between the oxide layer and the Zr-4 was obvious. Following this procedure, the zirconium oxide layer thickness can be measured accurately at different positions of cross section.
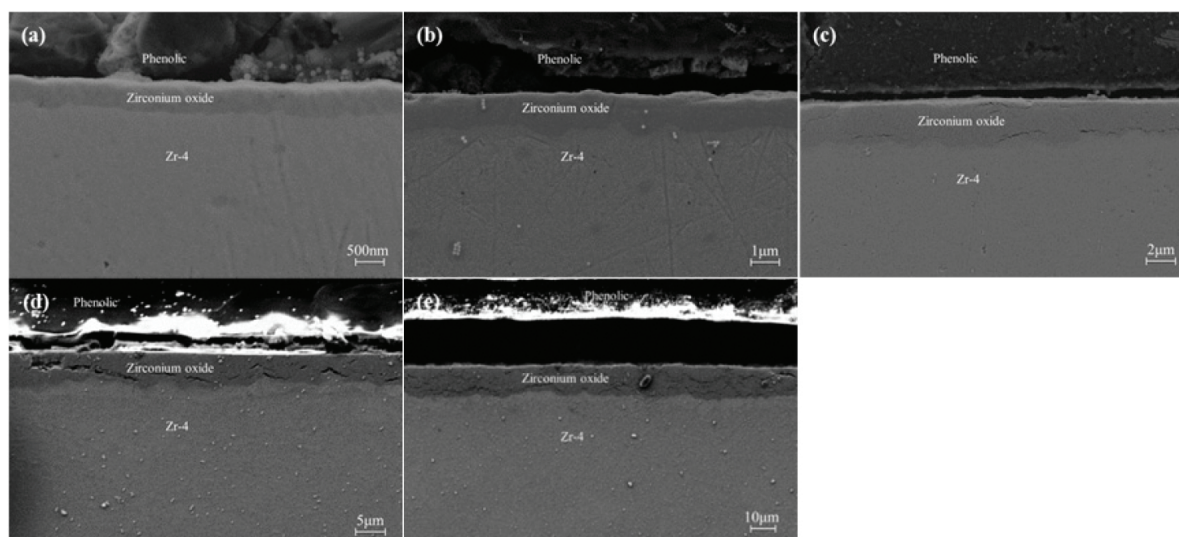

Figure 10. The cross-sectional SEM images of Zircaloy-4 samples oxidized at 500 °C in ambient air for (a) 5, (b) 10, (c) 20, (d) 50, and (e) 100 h. From Ref. [58].

The cross-sectional SEM images of the samples are shown in **Figure 10(a)–(e)**. The SEM images were taken in more than 20 different regions over the whole cross section of each sample, so they can be representative of the sample oxide layer thickness. The statistical average thickness and standard deviation of the top oxide layer are shown in **Figure 11**. The thickness of the oxide layer increases roughly linearly with oxidation time. For the 5 h sample, there is a very thin uniform oxide layer on the Zr-4. As the thickness increases, the top oxide layer becomes nonuniform, and the interface between zirconium oxide and Zr-4 becomes rougher. The average thickness of the oxide layer for the 5 h sample is about 0.55 μm with a deviation of about 0.066 μm. But for the 100 h sample, the average thickness of the oxide layer is about 10.13 μm with a deviation of about 3.08 μm. This suggests that during oxidation, the growth rate of the oxide layer varies across the sample, and the oxide layer will have an uneven profile.
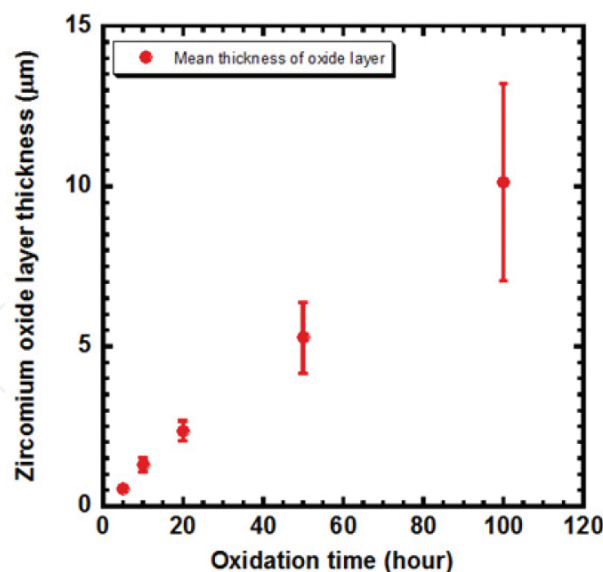
Figure 11. The calculated statistical average thickness and deviation of all oxidized samples as a function of oxidation time. From Ref. [58].

In order to analyze these two peaks quantitatively, the Gaussian-Lorentzian mode deconvolutions were carried out on two characteristic peaks around 180 and 630 cm^{-1}, which are candidate signals for detecting the Zr-4 cladding oxide layer thickness. **Figure 12** shows the deconvolution processes of these two characteristic peaks from the selected representative spectra of the 10 and 100 h samples. After deconvolution, the two sub-peaks can be replaced by individual peaks at the 175 and 187 cm^{-1} and 613 and 638 cm^{-1} positions, respectively. The intensities of these four peaks from the representative Raman spectra of all oxidized samples are shown in **Figure 12** as a function of the average thickness of the oxide layer. The intensities of these four deconvoluted peaks increase consistently as the oxide layer becomes thicker. For the 10 h sample with average oxide layer thickness of 1.30 μm, the intensities of the deconvoluted peaks are 44.1, 26.6, 21.3, and 39.5. For the 100 h sample with average oxide layer thickness of 10.13 μm, the intensities have increased greatly to 645.5, 405.5, 264.9, and 356.5.

The difference in intensities of the peaks at 175, 187, 613, and 638 cm^{-1} is able to identify each sample with the corresponding oxide layer thickness with high resolution as shown in **Figure 13**. Taking the peak at 175 cm^{-1} as an example, the peak intensity increases from 0 for a bare sample to 3.5, 44.1, 63.2, 186.6, and 645.5 for 0.55, 1.30, 2.36, 5.27, and 10.13 μm oxide layer thicknesses. Because there is no peak at these positions for the bare sample, it is easy to distinguish it from the oxidized samples, even for the 5 h sample with a 0.55 μm thick oxide layer. Among the oxidized samples, the average thickness difference between 5 and 10 h samples is only about 0.75 μm, but the signal intensity of the 10 h sample is almost 10 times higher than that of the 5 h sample. Another three peaks show similar trends. This result reflects that during the oxidation process at 500 °C, as oxidation time increases, the components of the tetragonal and monoclinic polymorph zirconium oxide become more, and consequently, they show much stronger characteristic peaks in the Raman spectra [44].
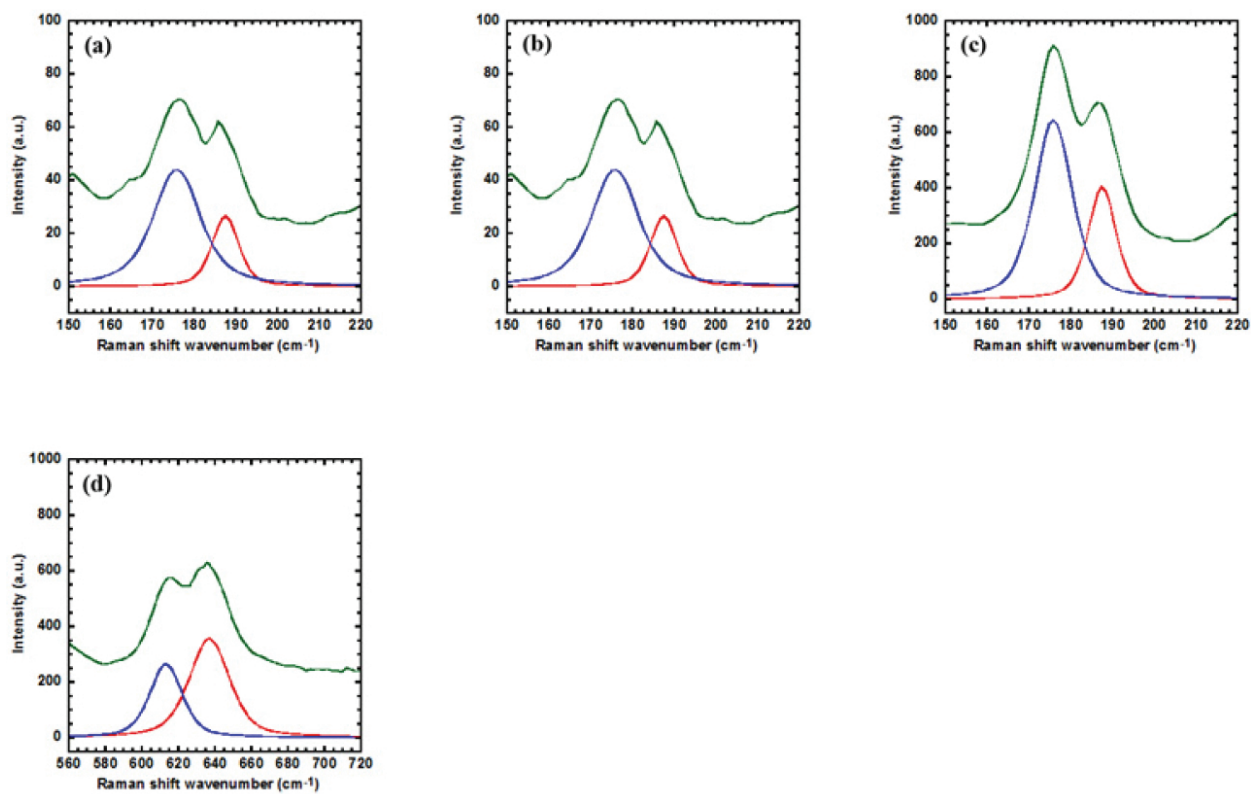
Figure 12. The Gaussian-Lorentzian deconvolution processes of characteristic peaks around 180 and 630 cm^{-1} from the selected representative Raman spectra of the 10 (a) (b) and 100 h (c) (d) oxidized samples. From Ref. [58].
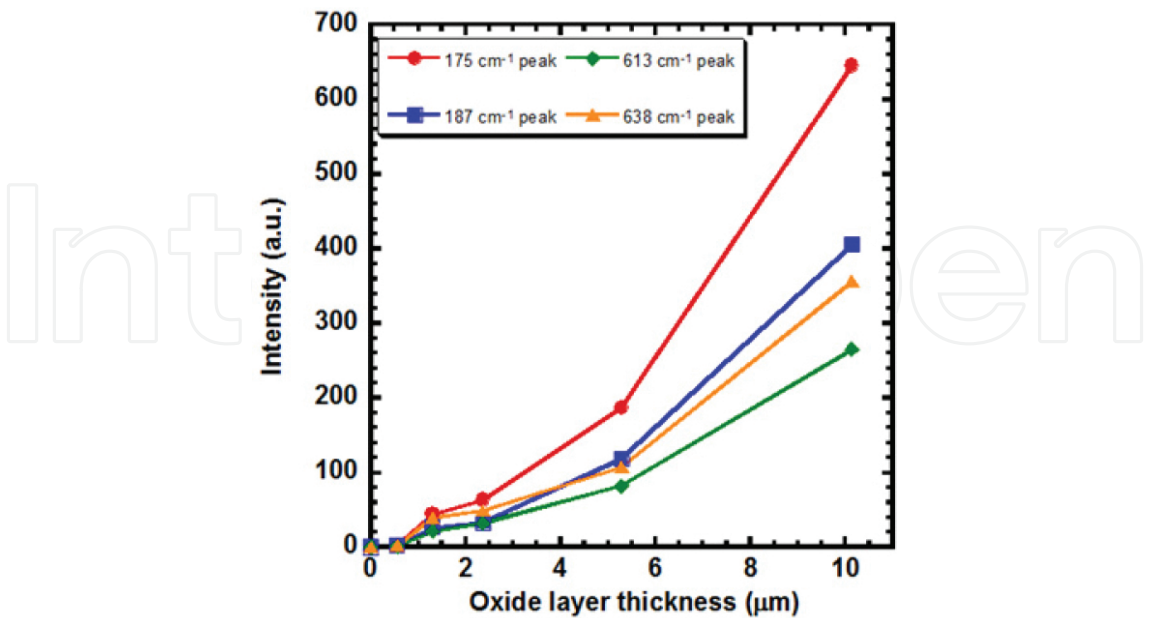

Figure 13. The intensities of the deconvoluted peaks at 175, 187, 613, and 638 cm^{-1} as a function of the average thickness of the oxide layer. From Ref. [58].

Figure 14 shows the maximum intensity deviation percentages of each characteristic peak from different test positions for all oxidized samples as a function of the average thickness of the oxide layer. It is observed that the maximum intensity deviations for these characteristic peaks are in the range from about 5 % to a little lower than 25 %. This intensity variation comes from the difference in the thickness of the oxide layer. This result means that the uneven condition of the oxide layer thickness for the sample can be roughly reflected in intensity variation of the characteristic peaks. After analysis of these characteristic peaks, they can be confidently considered as sufficient scattering signals to detect the oxide layer thickness on Zr-4 cladding and further employed to finish the task of converting the oxide layer thickness to detectable optical signals.
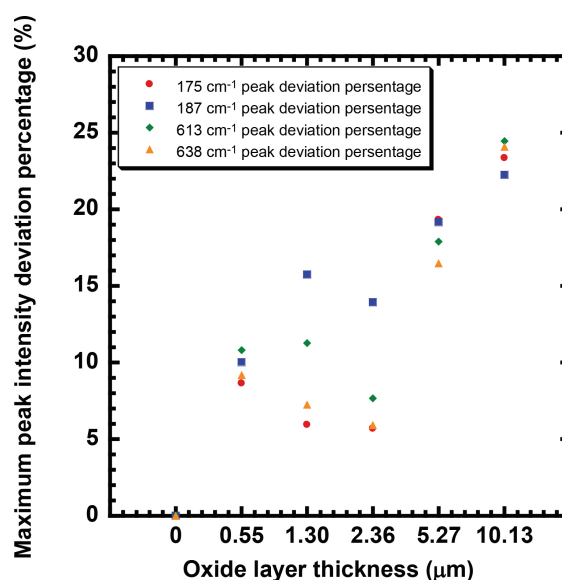

Figure 14. The maximum intensity deviation percentages of the characteristic peaks (deconvoluted) as a function of the average thickness of the oxide layer. From Ref. [58].

4. Conclusion

Raman spectroscopy has been demonstrated to successfully probe the tensile biaxial strain in monolayer graphene on the surface of SiO_2 nanopillars patterned by a self-assembled block copolymer. The characteristic Raman peaks of the G band and 2D band shifted due to the strain, and the Raman shifts accurately expressed the strain value distributed on graphene. The surface profile of the transferred graphene film on SiO_2 nanopillars was carefully investigated by AFM, and the biaxial tensile strain generated in the graphene was extracted from the physical deformation. Then, finite element simulations were used to validate the measurements. Both the AFM experimental investigation and FEM theory modeling matched the strain results achieved from Raman spectroscopy study and proved the capability of Raman scattering to monitor the subtle mechanical property change of graphene.

Raman scattering technology was studied to monitor spent fuel cladding oxidation. The air-oxidized Zr-4 cladding samples were systematically investigated by Raman spectroscopy. Straightforward Raman spectrum analysis reveals that there are characteristic peaks able to identify the bare and oxidized cladding samples and samples with different oxide layer thicknesses. SEM scans were carried out to visually examine oxide layer thicknesses on cladding. The comparison results confirmed this Raman scattering detection method displays high resolution in the determination of the oxidation corrosion degrees.

In summary, Raman scattering technology was proposed to monitor mechanical property of novel 2D carbon material and oxidation film thicknesses on nuclear fuel cladding Zircaloy. The positions and intensities of the characteristic peaks of the materials under test accurately and reliably revealed the changes in physical and chemical properties. The work reported in this chapter on observing materials with Raman spectroscopy extends the application of Raman scattering technology in monitoring new nanomaterial status and the health of nuclear storage systems in the research and engineering development.

Author details

Hongyi Mi[1], Zhenqiang Ma[1*] and James P. Blanchard[2]

*Address all correspondence to: mazq@engr.wisc.edu

1 Department of Electrical and Computer Engineering, University of Wisconsin-Madison, Madison-Wisconsin, United States of America

2 Department of Engineering Physics, University of Wisconsin-Madison, Madison-Wisconsin, United States of America

References

[1] W. H. Weber and R. Merlin, *Raman Scattering in Materials Science*. Springer-Verlag, Berlin Heidelberg, Germany 2000.

[2] S.-L. Zhang, *Raman Spectroscopy and its Application in Nanostructures*. John Wiley & Sons, Chichester, United Kingdom, 2012.

[3] A. Jorio, M. S. Dresselhaus, R. Saito, and G. Dresselhaus, *Raman Spectroscopy in Graphene Related Systems*. WILEY-VCH Verlag GmbH & Co. KGaA, Weinheim, Germany,2011.

[4] I. R. Lewis and H. Edwards, *Handbook of Raman Spectroscopy: From the Research Laboratory to the Process Line*. Marcel Dekker, Inc., New York, NY, United States of America, 2001.

[5] K. S. Novoselov, A. K. Geim, S. V. Morozov, D. Jiang, Y. Zhang, S. V. Dubonos, I. V. Grigorieva, and A. A. Firsov, "Electric field effect in atomically thin carbon films," *Science*, vol. 306, no. 5696, pp. 666–669, Oct. 2004.

[6] A. K. Geim and K. S. Novoselov, "The rise of graphene," *Nat. Mater.*, vol. 6, no. 3, pp. 183–191, Mar. 2007.

[7] K. S. Novoselov, A. K. Geim, S. V. Morozov, D. Jiang, M. I. Katsnelson, I. V. Grigorieva, S. V. Dubonos, and A. A. Firsov, "Two-dimensional gas of massless Dirac fermions in graphene," *Nature*, vol. 438, no. 7065, pp. 197–200, Nov. 2005.

[8] Y. Zhang, Y.-W. Tan, H. L. Stormer, and P. Kim, "Experimental observation of the quantum Hall effect and Berry's phase in graphene," *Nature*, vol. 438, no. 7065, pp. 201–204, Nov. 2005.

[9] K. I. Bolotin, K. J. Sikes, Z. Jiang, M. Klima, G. Fudenberg, J. Hone, P. Kim, and H. L. Stormer, "Ultrahigh electron mobility in suspended graphene," *Solid State Commun.*, vol. 146, no. 9–10, pp. 351–355, Jun. 2008.

[10] X. Du, I. Skachko, A. Barker, and E. Y. Andrei, "Approaching ballistic transport in suspended graphene," *Nat. Nanotechnol.*, vol. 3, no. 8, pp. 491–495, Aug. 2008.

[11] C. Lee, X. Wei, J. W. Kysar, and J. Hone, "Measurement of the elastic properties and intrinsic strength of monolayer graphene," *Science*, vol. 321, no. 5887, pp. 385–388, Jul. 2008.

[12] A. A. Balandin, S. Ghosh, W. Bao, I. Calizo, D. Teweldebrhan, F. Miao, and C. N. Lau, "Superior thermal conductivity of single-layer graphene," *Nano Lett.*, vol. 8, no. 3, pp. 902–907, Mar. 2008.

[13] R. R. Nair, P. Blake, A. N. Grigorenko, K. S. Novoselov, T. J. Booth, T. Stauber, N. M. R. Peres, and A. K. Geim, "Fine structure constant defines visual transparency of graphene," *Science*, vol. 320, no. 5881, pp. 1308–1308, Jun. 2008.

[14] Y.-M. Lin, C. Dimitrakopoulos, K. A. Jenkins, D. B. Farmer, H.-Y. Chiu, A. Grill, and P. Avouris, "100-GHz transistors from wafer-scale epitaxial graphene," *Science*, vol. 327, no. 5966, pp. 662–662, Feb. 2010.

[15] F. Bonaccorso, Z. Sun, T. Hasan, and A. C. Ferrari, "Graphene photonics and optoelectronics," *Nat. Photon.*, vol. 4, no. 9, pp. 611–622, Sep. 2010.

[16] F. Schwierz, "Graphene transistors," *Nat. Nanotechnol.*, vol. 5, no. 7, pp. 487–496, Jul. 2010.

[17] T. Sohier, M. Calandra, C.-H. Park, N. Bonini, N. Marzari, and F. Mauri, "Phonon-limited resistivity of graphene by first-principles calculations: electron-phonon interactions, strain-induced gauge field, and Boltzmann equation," *Phys. Rev. B*, vol. 90, no. 12, p. 125414, Sep. 2014.

[18] N. J. G. Couto, D. Costanzo, S. Engels, D.-K. Ki, K. Watanabe, T. Taniguchi, C. Stampfer, F. Guinea, and A. F. Morpurgo, "Random strain fluctuations as dominant disorder source for high-quality on-substrate graphene devices," *Phys. Rev. X*, vol. 4, no. 4, p. 041019, Oct. 2014.

[19] F. Guinea, M. I. Katsnelson, and A. K. Geim, "Energy gaps and a zero-field quantum Hall effect in graphene by strain engineering," *Nat. Phys.*, vol. 6, no. 1, pp. 30–33, Jan. 2010.

[20] N. Wei, L. Xu, H.-Q. Wang, and J.-C. Zheng, "Strain engineering of thermal conductivity in graphene sheets and nanoribbons: a demonstration of magic flexibility," *Nanotechnology*, vol. 22, no. 10, p. 105705, 2011.

[21] J. C. Meyer, A. K. Geim, M. I. Katsnelson, K. S. Novoselov, T. J. Booth, and S. Roth, "The structure of suspended graphene sheets," *Nature*, vol. 446, no. 7131, pp. 60–63, Mar. 2007.

[22] V. M. Pereira and A. H. Castro Neto, "Strain engineering of graphene's electronic structure," *Phys. Rev. Lett.*, vol. 103, no. 4, p. 046801, Jul. 2009.

[23] Z. H. Ni, T. Yu, Y. H. Lu, Y. Y. Wang, Y. P. Feng, and Z. X. Shen, "Uniaxial strain on graphene: Raman spectroscopy study and band-gap opening," *ACS Nano*, vol. 2, no. 11, pp. 2301–2305, Nov. 2008.

[24] C. Metzger, S. Rémi, M. Liu, S. V. Kusminskiy, A. H. Castro Neto, A. K. Swan, and B. B. Goldberg, "Biaxial strain in graphene adhered to shallow depressions," *Nano Lett.*, vol. 10, no. 1, pp. 6–10, Jan. 2010.

[25] A. C. Ferrari, J. C. Meyer, V. Scardaci, C. Casiraghi, M. Lazzeri, F. Mauri, S. Piscanec, D. Jiang, K. S. Novoselov, S. Roth, and A. K. Geim, "Raman spectrum of graphene and graphene layers," *Phys. Rev. Lett.*, vol. 97, no. 18, p. 187401, Oct. 2006.

[26] F. Ding, H. Ji, Y. Chen, A. Herklotz, K. Dörr, Y. Mei, A. Rastelli, and O. G. Schmidt, "Stretchable graphene: a close look at fundamental parameters through biaxial straining," *Nano Lett.*, vol. 10, no. 9, pp. 3453–3458, Sep. 2010.

[27] T. M. G. Mohiuddin, A. Lombardo, R. R. Nair, A. Bonetti, G. Savini, R. Jalil, N. Bonini, D. M. Basko, C. Galiotis, N. Marzari, K. S. Novoselov, A. K. Geim, and A. C. Ferrari, "Uniaxial strain in graphene by Raman spectroscopy: G peak splitting, Gr"uneisen parameters, and sample orientation," *Phys. Rev. B*, vol. 79, no. 20, p. 205433, May 2009.

[28] J. Zabel, R. R. Nair, A. Ott, T. Georgiou, A. K. Geim, K. S. Novoselov, and C. Casiraghi, "Raman spectroscopy of graphene and bilayer under biaxial strain: bubbles and balloons," *Nano Lett.*, vol. 12, no. 2, pp. 617–621, Feb. 2012.

[29] C. Metzger, S. Rémi, M. Liu, S. V. Kusminskiy, A. H. Castro Neto, A. K. Swan, and B. B. Goldberg, "Biaxial strain in graphene adhered to shallow depressions," *Nano Lett.*, vol. 10, no. 1, pp. 6–10, Jan. 2010.

[30] J. D. Werner, NRC: storage of spent nuclear fuel." *CRS. Rep. Congress*, May 2012.

[31] *Safety and Security of Commercial Spent Nuclear Fuel Storage: Public Report*. Washington, D.C.: National Academies Press, 2006.

[32] G. D. Moan and P. Rudling, *Zirconium in the Nuclear Industry: Thirteenth International Symposium*. ASTM International, West Conshohocken, PA, United States of America, 2002.

[33] D. G. Boase and T. T. Vandergraaf, "The Canadian spent fuel storage canister: some materials aspects," *Nucl. Technol.*, vol. 32, no. 1, pp. 60–71, Jan. 1977.

[34] J. S. Bryner, "The cyclic nature of corrosion of zircaloy-4 in 633 K water," *J. Nucl. Mater.*, vol. 82, no. 1, pp. 84–101, Jun. 1979.

[35] M. Suzuki and S. Kawasaki, "Oxidation of zircaloy cladding in air," *J. Nucl. Mater.*, vol. 140, no. 1, pp. 32–43, Aug. 1986.

[36] B. Cox, "Some thoughts on the mechanisms of in-reactor corrosion of zirconium alloys," *J. Nucl. Mater.*, vol. 336, no. 2–3, pp. 331–368, Feb. 2005.

[37] D. Shooter, "Chapter 3. Experimental methods for the study of heterogeneous reactions," in *Comprehensive Chemical Kinetics*, vol. 1, C. H. Bamford and C. F. H. Tipper, Ed. Elsevier, Amsterdam, the Netherlands, 1969, pp. 180–278.

[38] R. J. Grossman, "Continuous measurement of Zircaloy corrosion in air with an ultrasonic corrosion monitor," in *IEEE 1984 Ultrasonics Symposium*, 1984, pp. 860–865.

[39] I. S. Woolsey and J. R. Morris, "A study of Zircaloy-2 corrosion in high temperature water using ion beam methods," *Corrosion*, vol. 37, no. 10, pp. 575–585, Oct. 1981.

[40] K. Poulard, A. Chevarier, N. Moncoffre, P. Trocellier, and D. Crusset, "Study of zircaloy-4 fuel cladding corrosion using ion beams: application to long-term disposal of nuclear wastes," *Nucl. Instrum. Methods Phys. Res. Sect. B Beam Interact. Mater. At.*, vol. 181, no. 1–4, pp. 640–643, Jul. 2001.

[41] N. Ramasubramanian and V. C. Ling, "Fourier transform infrared reflection (FTIR) spectroscopy of corrosion films on irradiated zirconium alloys," *J. Nucl. Mater.*, vol. 175, no. 3, pp. 237–243, Dec. 1990.

[42] B. Cox and W. Yin-Mei, "Direct measurement of the thickness and optical properties of zirconia corrosion films," *J. Nucl. Mater.*, vol. 199, no. 3, pp. 258–271, Feb. 1993.

[43] I. Idarraga, M. Mermoux, C. Duriez, A. Crisci, and J. P. Mardon, "Raman investigation of pre- and post-breakaway oxide scales formed on Zircaloy-4 and M5® in air at high temperature," *J. Nucl. Mater.*, vol. 421, no. 1–3, pp. 160–171, Feb. 2012.

[44] V. G. Keramidas and W. B. White, "Raman scattering study of the crystallization and phase transformations of ZrO_2," *J. Am. Ceram. Soc.*, vol. 57, no. 1, pp. 22–24, Jan. 1974.

[45] R. Srinivasan, M. B. Harris, S. F. Simpson, R. J. De Angelis, and B. H. Davis, "Zirconium oxide crystal phase: the role of the pH and time to attain the final pH for precipitation of the hydrous oxide," *J. Mater. Res.*, vol. 3, no. 04, pp. 787–797, Aug. 1988.

[46] P. Barberis, T. Merle-Méjean, and P. Quintard, "On Raman spectroscopy of zirconium oxide films," *J. Nucl. Mater.*, vol. 246, no. 2, pp. 232–243, Aug. 1997.

[47] P. Barbéris, G. Corolleur-Thomas, R. Guinebretière, T. Merle-Mejean, A. Mirgorodsky, and P. Quintard, "Raman spectra of tetragonal zirconia: powder to zircaloy oxide frequency shift," *J. Nucl. Mater.*, vol. 288, no. 2–3, pp. 241–247, Feb. 2001.

[48] P. E. Quintard, P. Barbéris, A. P. Mirgorodsky, and T. Merle-Méjean, "Comparative lattice-dynamical study of the Raman spectra of monoclinic and tetragonal phases of zirconia and hafnia," *J. Am. Ceram. Soc.*, vol. 85, no. 7, pp. 1745–1749, Jul. 2002.

[49] J. S. Moya, M. Diaz, J. F. Bartolomé, E. Roman, J. L. Sacedon, and J. Izquierdo, "Zirconium oxide film formation on zircaloy by water corrosion," *Acta Mater.*, vol. 48, no. 18–19, pp. 4749–4754, Dec. 2000.

[50] R. Ruiz, H. Kang, F. A. Detcheverry, E. Dobisz, D. S. Kercher, T. R. Albrecht, J. J. de Pablo, and P. F. Nealey, "Density multiplication and improved lithography by directed block copolymer assembly," *Science*, vol. 321, no. 5891, pp. 936–939, Aug. 2008.

[51] A. J. Hong, C.-C. Liu, Y. Wang, J. Kim, F. Xiu, S. Ji, J. Zou, P. F. Nealey, and K. L. Wang, "Metal nanodot memory by self-assembled block copolymer lift-off," *Nano Lett.*, vol. 10, pp. 224–229, Jan. 2010.

[52] H. Mi, S. Mikael, C.-C. Liu, J.-H. Seo, G. Gui, A. L. Ma, P. F. Nealey, and Z. Ma, "Creating periodic local strain in monolayer graphene with nanopillars patterned by self-assembled block copolymer," *Appl. Phys. Lett.*, vol. 107, no. 14, p. 143107, Oct. 2015.

[53] X. Li, W. Cai, J. An, S. Kim, J. Nah, D. Yang, R. Piner, A. Velamakanni, I. Jung, E. Tutuc, S. K. Banerjee, L. Colombo, and R. S. Ruoff, "Large-area synthesis of high-quality and uniform graphene films on copper foils," *Science*, vol. 324, no. 5932, pp. 1312–1314, Jun. 2009.

[54] K. S. Kim, Y. Zhao, H. Jang, S. Y. Lee, J. M. Kim, K. S. Kim, J.-H. Ahn, P. Kim, J.-Y. Choi, and B. H. Hong, "Large-scale pattern growth of graphene films for stretchable transparent electrodes," *Nature*, vol. 457, no. 7230, pp. 706–710, Feb. 2009.

[55] G. Grimvall, *Thermophysical Properties of Materials*. Elsevier, Amsterdam, the Netherlands, 1999.

[56] E. Cadelano, P. L. Palla, S. Giordano, and L. Colombo, "Nonlinear elasticity of monolayer graphene," *Phys. Rev. Lett.*, vol. 102, no. 23, p. 235502, Jun. 2009.

[57] C. M. Phillippi and K. S. Mazdiyasni, "Infrared and Raman spectra of zirconia poly-morphs," *J. Am. Ceram. Soc.*, vol. 54, no. 5, pp. 254–258, May 1971.

[58] H. Mi, S. Mikael, T. Allen, K. Sridharan, D. Butt, J. P. Blanchard, and Z. Ma, "Monitoring the oxidation of nuclear fuel cladding using Raman spectroscopy," *J. Nucl. Mater.*, vol. 445, no. 1–3, pp. 7–11, Feb. 2014.